Optimal Eco-Driving Control of Autonomous and Electric Trucks in Adaptation to Highway Topography: Energy Minimization and Battery Life Extension

Yongzhi Zhang, *Member, IEEE*, Xiaobo Qu, *Senior Member, IEEE*, and Lang Tong, *Fellow, IEEE*

***Abstract*— This article develops a model to plan energy-efficient speed trajectories of electric trucks in real time by considering the information of topography and traffic ahead of the vehicle. In this real-time control model, a novel state-space model is first developed to capture vehicle speed, acceleration, and state of charge. An energy minimization problem is then formulated and solved by an alternating direction method of multipliers (ADMM) that exploits the structure of the problem. A model predictive control (MPC) framework is further employed to deal with topographic and traffic uncertainties in real time. An empirical study is finally conducted on the performance of the proposed eco-driving algorithm and its impact on battery degradation. The simulation results show that the energy consumption by using the developed method is reduced by up to 5.05%, and the battery life is extended by more than 100% compared to benchmarking solutions.**

***Index Terms*— Alternating direction method of multipliers (ADMM), autonomous and electric trucks, battery life extension, energy minimization, heavy-duty (HDT) truck, model predictive control (MPC), speed control.**

I. Introduction

HEAVY-DUTY trucks (HDTs) account for 70% of all freight transport and 20% of transportation-sector greenhouse gas (GHG) emissions in the USA [1]. Therefore, the decarbonization of HDTs is essential for developing sustainable transportation and one technology that could deliver this is the battery-electric (BE) HDT [2], [3]. The electrification of HDT has developed greatly in recent years, and according to McKinsey, it was reported that BE trucks could account for 15% of global truck sales by 2030 [4]. However, the development of BE HDT is greatly limited to the present lithium-ion battery technology, especially due to the low energy density and short cycle life [5].

One way to address this technology bottleneck is to develop the next-generation battery with largely improved energy density and cycle life [6], which, however, generally requires decades and cannot meet the requirement of immediate usage. Another way is to reduce vehicle energy consumption and battery aging through intelligent energy management and speed control strategies, which is owed to the eco-driving control techniques. Indeed, many algorithms have been developed for the eco-driving of both passenger vehicles [7]–[10] and HDTs [11]–[15]. In [7], eco-driving techniques were discussed and formulated as an optimal control problem that consisted of the minimization of the vehicle consumption over a time and distance horizon, and then, a closed-form solution of the optimal trajectories was derived. Xu *et al.* [8] proposed a cooperative method of traffic signal control and vehicle speed optimization for connected automated vehicles, which optimized the traffic signal timing and vehicles' speed trajectories at the same time. Zeng and Wang [9] proposed an optimal speed planning solution for a vehicle running on a given route with multiple stop signs, traffic lights, and so on. Malikopoulos *et al.* [10] addressed the problem of speed control of a number of automated vehicles before they entered a speed reduction zone on a freeway. Although involving different driving scenarios with traffic signals, speed limits, and so on [7]–[10], for model simplification purposes, the passenger vehicle modeling generally neglects the impacts of road topographies and aerodynamics, which greatly affects the energy consumption of HDTs featured with a heavy and large body [16]. Some literature developed battery aging-conscious energy management strategies for hybrid electric vehicles (HEVs) by optimally splitting the driving power [17]–[20], but how to drive the electric vehicles (EVs) in an energy-efficient way with minimized battery aging still remains an open problem. In fact, due to the long-haul driving requirement, the shortcomings of batteries, such as low energy density and short cycle life, are greatly enlarged with the BE HDT. An eco-driving algorithm considering battery aging is thus especially required for the BE HDT optimal control.

The eco-driving control of HDTs is mainly focused on the internal combustion engine (ICE)-powered HDTs.

Manuscript received July 16, 2021; revised September 23, 2021 and December 28, 2021; accepted January 21, 2022. Date of publication January 31, 2022; date of current version April 20, 2022. This work was supported in part by Chalmers AoA Transport, in part by the Joint Programming Initiative Urban Europe (JPI EU) project SMUrTS, and in part by the Research Start-Up Funding of Chongqing University under Grant 02090011044160. *(Corresponding authors: Yongzhi Zhang; Xiaobo Qu.)*

Yongzhi Zhang is with the College of Mechanical and Vehicle Engineering, Chongqing University, Chongqing 400044, China, and also with the Department of Architecture and Civil Engineering, Chalmers University of Technology, 41296 Gothenburg, Sweden (e-mail: yzzhangbit@gmail.com).

Xiaobo Qu is with the Department of Architecture and Civil Engineering, Chalmers University of Technology, 41296 Gothenburg, Sweden (e-mail: xiaobo@chalmers.se).

Lang Tong is with the School of Electrical and Computer Engineering, Cornell University, Ithaca, NY 14853 USA (e-mail: lt35@cornell.edu).

Digital Object Identifier 10.1109/TTE.2022.3147214

TABLE I
SEGMENT VARIABLES DEFINITION FOR SEGMENT i

Notation	Definition	Explanation
T_i	The travel time trough segment i	-
t_i	The starting time of segment i	$t_1 = 0, t_{i+1} = t_i + T_i$
$v_i(t)$	The instantaneous EV velocity in segment i	$t_i < t < t_{i+1}$
x_i	The initial velocity at the beginning of segment i	$x_i = v_i(t_i)$, it is the system state.
a_i	The EV acceleration in segment i	This value is the system input and assumed to be constant in the short segment.
$p_i(t)$	The instantaneous power of the battery output in segment i	Negative in charging and positive in discharging.
$I_i(t)$	The instantaneous current of the battery output in segment i	Negative in charging and positive in discharging.
y_i	The SOC change in segment i	This value is the system output.

Hellström *et al.* [11] developed a predictive cruise controller where the dynamic programming (DP) method was used to solve the optimal control problem numerically. In [11], a preprocessing algorithm was developed to downsize the search space of DP so that the algorithm complexity was reduced for real-time operation. Guo and Wang [12] investigated the problem of speed planning and tracking control of a platoon of trucks and presented a two-layered hierarchical framework for truck platoon coordination: a speed planning layer for en route speed profile calculation and a control layer for vehicle speed tracking. Held *et al.* [13] developed fuel-efficient driving algorithms for applications with varying speed limits in urban driving, while Borek *et al.* [14] developed economic optimal control strategies with traffic involved and navigation at signalized intersections by using infrastructure-to-vehicular communication. The speed control of traditional HDT generally involves the optimization of gear selections (integer) when the DP method is often introduced [11], [12], [14], [15]. Compared to traditional HDTs, the speed control of BE HDT generally involves noninteger optimization, which thus provides the chance for introducing more efficient optimization algorithms than the DP method. To the best of the authors' knowledge, this is the first article focused on the optimal eco-driving control of BE HDT, considering impacts of both the energy consumption and battery aging.

In this work, three major contributions are made. First, a novel state-space model is constructed to capture the dependencies of vehicle speed, acceleration, and battery state of charge (SOC). Based on this model, the optimization problem for energy minimization is further formulated, with both road topographies and surrounding traffic involved. Then, a model predictive control (MPC) approach based on an alternating direction method of multipliers (ADMM) is developed by considering topographical and traffic uncertainties so that the efficient real-time speed control is realized. Finally, effects of the speed control algorithm on battery degradation are systematically evaluated by introducing an EV-oriented (battery) aging model, and an empirical study is further conducted to validate the performance of the eco-driving strategy with and without surrounding traffic.

The rest of this article is organized as follows. Section II describes a state-space model describing truck system dynamics. Section III defines the energy optimization problem and develops optimization and control algorithms. Section IV shows the truck energy consumption results based on the developed method, followed by Section V showing the battery aging evaluation results. Finally, Section VI concludes this article.

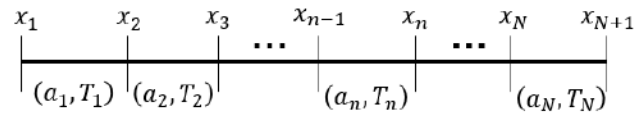

Fig. 1. Schematic.

II. STATE-SPACE EQUATION MODELING

In this section, a state-space model connecting the vehicle speed, acceleration, and energy consumption is constructed, where the vehicle speed and battery SOC are the model state and output, respectively. The modeling processes are presented in detail as follows.

Let the total trip be divided into N equally spaced segments of unit length, and segment i begins at t_i. The schematic is shown in Fig. 1 and the definition of segment variables is listed in Table I.

The state-space model is defined as

$$x_{i+1} = F_i(x_i, a_i), \quad y_i = G_i(x_i, a_i)$$

where $F_i(\cdot,\cdot)$ is the state transition and $G_i(\cdot,\cdot)$ is the output function.

A. State Transition Function

Note that the length of each road segment in Fig. 1 is considered as unit length "1" for easy derivation purposes, but it will be parameterized in the empirical studies (Section IV) based on the practical conditions. In this case, x_i, a_i, and T_i are related by

$$\int_0^{T_i} (x_i + a_i t)\, dt = 1 \Rightarrow a_i T_i^2 + 2x_i T_i - 2 = 0 \tag{1}$$

which gives

$$a_i = \frac{2}{T_i^2} - \frac{2x_i}{T_i}, \quad T_i = \frac{-x_i + \sqrt{x_i^2 + 2a_i}}{a_i}.$$

The state transition is then given by

$$x_{i+1} = x_i + a_i T_i = \sqrt{x_i^2 + 2a_i} \Rightarrow F_i(x_i, a_i) = \sqrt{x_i^2 + 2a_i}. \tag{2}$$

B. Output Function

1) SOC Change Within Each Road Segment: SOC indicates the ratio of battery remaining capacity to nominal capacity, and thus, the SOC change within each road segment is defined as

$$y_i = G_i(x_i, a_i) = \frac{\int_0^{T_i} I_i(t)\,dt}{C} = \frac{\int_0^{T_i} p_i(t)\,dt}{UC} \tag{3}$$

where C represents the battery nominal capacity and U represents the battery terminal voltage that is assumed constant within the commonly used SOC ranges [21].

2) Longitudinal Dynamics of Vehicle: The equation describing the longitudinal dynamics of vehicles is shown as

$$F_i^{\text{track}}(t) - F_i^{\text{air}}(t) - F_i^{\text{res}} = ma_i \tag{4}$$

with

$$\begin{cases} F_i^{\text{air}}(t) = \dfrac{1}{2}\rho_{\text{air}} A_{\text{f}} C_{\text{D}} v_i^2(t) \\ F_i^{\text{res}} = mgC_{\text{r}}\cos(\alpha_i) + mg\sin(\alpha_i) \end{cases}$$

where m is the vehicle mass; $F_i^{\text{track}}(t)$ is the track force generated by the electric motor (EM); $F_i^{\text{air}}(t)$ is the air resistance with ρ_{air} indicating the air mass density, A_{f} indicating the vehicle frontal area, and C_{D} indicating the aerodynamic drag coefficient; and F_i^{res} is the resistance consisting of the road frictional resistance and the gravitational resistance with C_{r} indicating the rolling resistance factor and α_i indicating the slope of segment i. To simplify the derivation process, it is assumed that $\beta^{\text{air}} = (1/2)\rho_{\text{air}} A_{\text{f}} C_{\text{D}}$ and $F_i^{\text{res}} = \beta_i^{(0)}$, where β^{air} is independent of road segment conditions, while $\beta_i^{(0)}$ depends on the slope of each road segment.

3) Output Function Modeling: The track force $F_i^{\text{track}}(t)$ is produced by the battery power. When the battery discharges, $p_i(t) > 0$, the electric power is converted to positive track force according to

$$F_i^{\text{track}}(t) = \beta^+ p_i(t)/v_i(t)$$

where β^+ indicates the vehicle discharging efficiency.

When the battery is charged by the kinetic energy, $p_i(t) < 0$, the motor produces negative track force as

$$F_i^{\text{track}}(t) = \beta^- p_i(t)/v_i(t)$$

where $1/\beta^-$ indicates the vehicle charging efficiency. Here, we assume that all the brakings can be accommodated through the electric brakes and are regenerative brakings; thus, friction braking is not included. This assumption is consistent with the practice, where the use of friction brakes is minimized to improve energy efficiency and reduce wear [22].

Then, the instantaneous battery power output is expressed as

$$p_i(t) = \frac{1}{\beta_i} v_i(t) F_i^{\text{track}}(t), \quad \beta_i = \begin{cases} \beta^+, & F_i^{\text{track}} \geq 0 \\ \beta^-, & \text{otherwise} \end{cases} \tag{5}$$

where β_i includes the efficiencies of the battery charging/discharging, the ac/dc converter, the EM, and the transmission gearbox. The transmission energy losses caused by the gearbox are small and the transmission energy efficiency is set to a constant close to 100% [15]. The EM efficiency varies as the torque and rotational speed of the motor, which can also be considered a constant based on the motor efficiency map and the vehicle speed limit in this study. The detailed simplification process of the EM efficiencies is presented in Appendix A.

Note that the sign of track force can be verified from (4), and thus, whether β_i equals β^+ or β^- is determined by the vector of (x_i, a_i), that is, the track force can be positive, negative, changing from positive to negative, or vice versa within each road segment. These four cases lead to different modeling processes of output function, which are presented in detail in Appendix B.

Generally, the output function can be expressed as

$$G_i(x_i, a_i) = \gamma_i^{(0)} + \gamma_i^{(1)} a_i + \gamma_i^{(2)} x_i^2$$

where the expressions of vector $\gamma_i(x_i, a_i)$ are concluded in Table V (Appendix B).

III. Formulation and Solution of the Energy Minimization Problem

A. Problem Formulation of Energy Minimization

The total energy consumed (E) is given by the cumulative SOC change. In this case,

$$E = \sum_{i=1}^{N+1} \left(\gamma_i^{(0)} + \gamma_i^{(1)} a_i + \gamma_i^{(2)} x_i^2 \right). \tag{6}$$

From (1) and (2), there is

$$\begin{cases} x_{i+1} = x_i + a_i T_i \\ a_i T_i^2 + 2x_i T_i - 2 = 0 \end{cases} \Rightarrow \begin{cases} a_i = \dfrac{x_{i+1}^2 - x_i^2}{2} \\ \dfrac{1}{T_i} = \dfrac{x_{i+1} + x_i}{2}. \end{cases}$$

By substituting a_i in the total energy expression, there is

$$E = \eta_0(x) + \sum_{i=1}^{N+1} \eta_i(x) x_i^2 \tag{7}$$

where $x = [x_1, x_2, \ldots, x_{N+1}]^\top$ and

$$\begin{cases} \eta_0(x) = \displaystyle\sum_{i=1}^{N} \gamma_i^{(0)} \\ \eta_i(x) = \begin{cases} \gamma_1^{(2)} - \dfrac{\gamma_1^{(1)}}{2}, & i = 1 \\ \gamma_i^{(2)} - \dfrac{\gamma_i^{(1)}}{2} + \dfrac{\gamma_{i-1}^{(1)}}{2}, & i = 2, 3, \ldots, N \\ \dfrac{\gamma_N^{(1)}}{2}, & i = N+1. \end{cases} \end{cases}$$

The minimum energy control is to minimize the energy consumption subject to a total trip-time constraint τ and the

optimization problem $\mathcal{P}^{\mathrm{ME}}$ is thus formulated as

$$\begin{aligned}\underset{T_i\geq 0, x_i\geq 0}{\text{minimize}}\ & J^{\mathrm{ME}}(x)=\eta_0(x)+\sum_{i=1}^{N+1}\eta_i(x)x_i^2\\ \text{s.t.}\ & \sum_{i=1}^{N}T_i=\tau,\quad i=1,\ldots,N\\ & T_ix_i+T_ix_{i+1}=2,\quad i=1,\ldots,N\\ & \underline{x}_i\leq x_i\leq \bar{x}_i,\quad i=1,\ldots,N+1\end{aligned}$$

where $\underline{x}_i$ and $\bar{x}_i$ are, respectively, the lower and upper speed limits, and the traffic information can be introduced easily by adapting the speed limits to surrounding traffic. Note that $\mathcal{P}^{\mathrm{ME}}$ involves two sets of variables, including the speed x and the travel time T to be optimized. Although the above optimization is nonconvex, optimizing x for fixed T can be solved easily. For fixed x, solving T that satisfies the constraints amounts to solving a linear equation. Thus, a method of alternately solving x and T can be derived accordingly.

B. ADMM-Based Optimal Solution

The ADMM is a simple but powerful algorithm that is well suited to distributed optimization problems as described in $\mathcal{P}^{\mathrm{ME}}$. It takes the form of a decomposition-coordination procedure, in which the solutions to small local subproblems are coordinated to find a solution to a large global problem. ADMM can be viewed as an attempt to blend the benefits of dual decomposition and augmented Lagrangian methods for constrained optimization [23].

As in the method of multipliers, the augmented Lagrangian is formed by relaxing the constraints in $\mathcal{P}^{\mathrm{ME}}$ as

$$\begin{aligned}\tilde{L}(x,T,\mu,\lambda,\rho)=\eta_0(x)&+\sum_i\eta_i(x)x_i^2+\lambda\left(\sum_i T_i-\tau\right)\\&+\sum_i\mu_i(T_ix_i+T_ix_{i+1}-2)\\&+\frac{\rho_1}{2}\left(\sum_i T_i-\tau\right)^2\\&+\sum_i\frac{\rho_{2i}}{2}(T_ix_i+T_ix_{i+1}-2)^2\end{aligned}\tag{8}$$

where $\mu=[\mu_1,\mu_2,\ldots,\mu_N]^\top$ and λ are the Lagrange multipliers associated with constraints in $\mathcal{P}^{\mathrm{ME}}$ and $\rho=[\rho_1,\rho_{21},\rho_{22},\cdots,\rho_{2N}]^\top$ are the penalty coefficients.

Minimizing the Lagrangian (8) with respect to (x,T) is nontrivial. The difficulty can be lessened considerably if x and T are solved separately, which gives rise to an iterative approach to solving $\mathcal{P}^{\mathrm{ME}}$. In particular, when the speed trajectory x is fixed, $\eta_0(x)$ and $\eta_i(x)$ are determined. Equation (8) can thus be expressed as a quadratic function of T

$$\tilde{L}=T^\top A(x,\rho)T+T^\top b(x,\mu,\lambda,\rho)+c(x,T,\mu,\lambda,\rho)\tag{9}$$

where $T=[T_1,T_2,\cdots,T_N]^\top$, $A\in\mathcal{R}^{N\times N}$ is a matrix coefficient of the quadratic term, $b\in\mathcal{R}^N$ is a vector coefficient of the first-order term, and $c\in\mathcal{R}$ is a constant. Minimizing the Lagrangian with respect to T can be obtained in closed form. The ADMM algorithm to solve $\mathcal{P}^{\mathrm{ME}}$ is shown in Algorithm 1.

Algorithm 1 ADMM Algorithm Is Given by the Following Iterations

1: Initialize μ,λ,ρ, the speed trajectory $x^{(0)}$, and the trip time $T^{(0)}$.
2: **repeat**
3: Solve the primal variables:

$$x^{(n+1)}=\operatorname{argmin}\tilde{L}\left(x,T^{(n)},\mu^{(n)},\lambda^{(n)},\rho\right)\tag{10}$$

$$\begin{aligned}T^{(n+1)}&=\operatorname{argmin}\tilde{L}\left(x^{(n+1)},T,\mu^{(n)},\lambda^{(n)},\rho\right)\\&=-\frac{1}{2}A^{-1}\left(x^{n+1},\rho\right)b\left(x^{(n+1)},\mu^{(n)},\lambda^{(n)},\rho\right).\end{aligned}\tag{11}$$

4: Update the multipliers:

$$\lambda^{(n+1)}=\lambda^{(n)}+\rho\left(\sum_i T_i^{(n+1)}-\tau\right)\tag{12}$$

$$\begin{aligned}\mu_i^{(n+1)}=\mu_i^{(n)}+\rho_{2i}\Big(&T_i^{(n+1)}x_i^{(n+1)}\\&+T_i^{(n+1)}x_{i+1}^{(n+1)}-2\Big).\end{aligned}\tag{13}$$

5: **until** the solution difference between two iterations is small enough with $\|x^{(n+1)}-x^{(n)}\|_2+\|T^{(n+1)}-T^{(n)}\|_2\leq\varepsilon_1$ and the constraints of the optimization problem are met with $\|(\sum_i T_i^{(n+1)}-\tau)+\sum_i(T_i^{(n+1)}x_i^{(n+1)}+T_i^{(n+1)}x_{i+1}^{(n+1)}-2)\|_2\leq\varepsilon_2$, where ε_1 and ε_2 are two predefined positive real numbers close to zero.

Note that (10) that updates $x^{(n)}$ to $x^{(n+1)}$ can either solved by a standard solver or, perhaps more easily for a large problem, by first-order (gradient) updates.

Also, note that the sign of track force will not change suddenly as the speed trajectory x gradually changes. A positive track force within road segment i changes gradually as that in Case III (Appendix B) before finally turning into a negative track force. In other words, the sign change of track force for each road segment actually represents the move of zero track force point (see Fig. 16 in Appendix B). The continuity of track force determines the continuity of energy consumption in feasible solutions.

Suppose that there is a feasible solution x_0 and the vector parameter $\gamma_i(x_0)$ is determined accordingly, and there will be $\lim_{x\to x_0}\gamma_i(x)=\gamma_i(x_0)$. Because $\eta_i(x)$ consists of $\gamma_i(x)$, there will also be $\lim_{x\to x_0}\eta_i(x)=\eta_i(x_0)$. Since x_0 can be any feasible solution, the objective function is continuous in the feasible solutions of x, which guarantees the local convergence of the proposed algorithm. In our simulation, it is observed that convergence happens approximately (or on average) in 50–100 iterations.

C. MPC-Based Vehicle Speed Control

MPC is a rolling-window closed-loop control that incorporates real-time operating conditions. For optimal BE HDT control, MPC solves an N-segment open-loop control and implements only the control of the first segment [24]. Fig. 2 shows the information flow of the MPC framework.

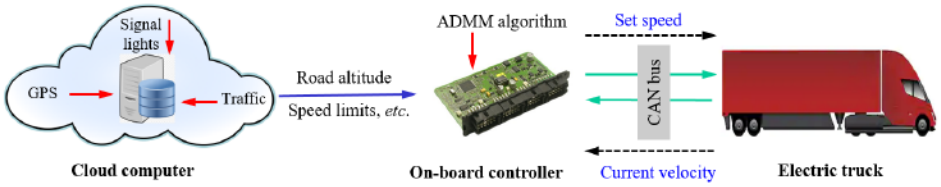

Fig. 2. Information flow of the MPC framework.

TABLE II
SPECIFICATIONS OF THE TESLA SEMI TRUCK AND BATTERY PACK

Parameters	Description	Value
m	Vehicle mass	40,000 kg
C_r	Rolling resistance coefficient with tyre type	0.0055
A_f	The frontal area	10 m^2
C_D	Aerodynamic drag coefficient	0.36
E_T	Nominal energy in total	250 kWh *4
U	Nominal voltage (one battery pack)	800 V
C	Nominal capacity (one battery pack)	312.5 Ah
β^+	Vehicle discharge efficiency (battery to wheel)	0.85
$\frac{1}{\beta^-}$	Vehicle charge efficiency (wheel to battery)	0.80

A cloud-based platform for traffic information and situational awareness sends the updated information to the onboard controller, including road altitudes, speed limits, accidents, and emergencies ahead. Based on the traffic information from the cloud platform and local sensing results (such as the distance of the car in front of the truck), the embedded ADMM algorithm calculates the optimal velocity and trip time within a small number of limited road segments, say $N = 30$. Only the velocity of the first segment is executed in truck operation. Note that the accurate road topographies and speeds of the preceding vehicle required by the onboard controller in this research are assumed to be available. The road grades can be estimated by fusion of GPS and vehicle real-time data, with measurements from previous runs over the same road segment [25]. The preceding vehicle trajectory can be planned or computed by the preceding vehicle and communicated to the following one [7], [8], [12], [13] or they can be computed by the following vehicle itself by exploring past and present measures of the distance and relative speed collected by onboard sensors [26], [27].

IV. CASE STUDY

Simulations were performed on the road data of highway E4 between the cities of Södertälje and Norrköping in Sweden [11]. The road slope and altitude are shown in Fig. 3. The electric truck modeled was a Tesla Semi tractor and trailer. The specifications of the truck and battery pack [2] are given in Table II. Note that the truck had four separate motors to drive the front four wheels individually, and each motor was powered by a battery pack with the nominal voltage and capacity being, respectively, 800 V and 312.5 Ah.

Algorithm parameters were initialized as follows. The length of each road segment l was set to 50 m, and the number of segments N was set to 30. The setting of 50-m length

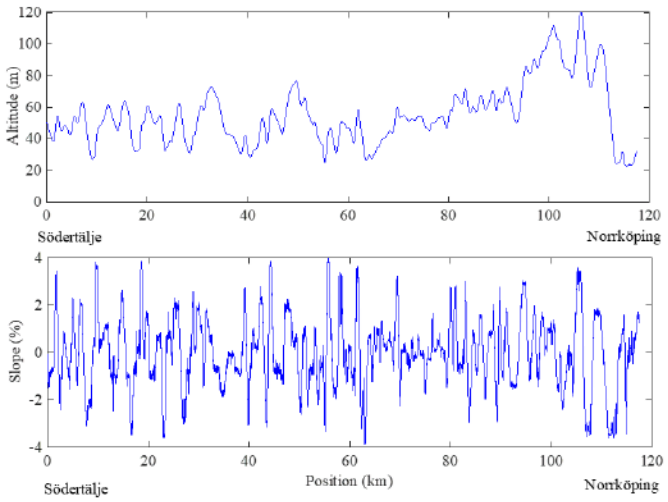

Fig. 3. Estimated road topography (altitude and slope) from Södertälje to Norrköping.

for each segment, whose value can be adjusted according to practical conditions, has been proven to be feasible in practice [11], [28]. Therefore, the prediction horizon was 1500 m. The speed lower bound was set to 0 km/h. In the case without traffic involved, the speed upper bound was set to the EU legal maximum of 90 km/h and the speed lower bound was set to 75 km/h [11], while in the case under traffic, the speed was limited to surrounding traffic. Simulations were conducted in the environment of MATLAB 2020a based on a Macbook Pro with a processor of 8-Core Intel Core i9 @2.4 GHz and a memory of 32 GB.

A. Optimal Speed Control Without Traffic Involved

In this case, the trip time τ was set equal to the trip time of that using a uniform speed of 85 km/h to travel through the same distance.

1) Overall Performance: Two simulations were conducted based on the road data between Södertälje and Norrköping to compare the performance of the ADMM controller and the uniform speed cruise control (CC) controller. The CC speed was set at 85 km/h, and the relative changes of energy consumption and trip time between the two controllers are shown in Fig. 4. A negative value indicates that the ADMM controller has a lower value than the CC does. The results show that, compared to the CC, the ADMM controller saved 4.28% energy from Södertälje to Norrköping and 4.83% energy from the return, while the trip time between these two controllers was similar to each other in both directions.

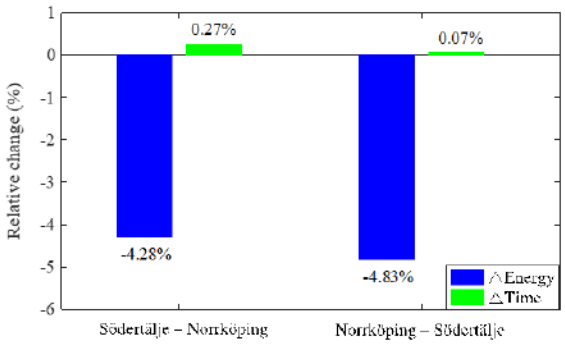

Fig. 4. Simulation results on the road data from Södertälje to Norrköping and the return.

2) Performance Comparison: Since there is no published work on energy-efficient eco-driving of BE HDT, the comparisons were made with energy-efficient driving algorithms for traditional trucks [11] where DP and proportional–integral control (PIC) were proposed. Also, the optimal speed trajectories from [11] are directly introduced for performance comparisons. According to [11], the PIC is a standard controller available from Scania. All parameters that could affect the vehicle energy consumption were set to the same as those in [11]. Fig. 5 presents the comparison results between ADMM, DP, PIC, and CC based on the road slopes in [11, Figs. 7 and 9]. The speed value of the CC was set to have the same trip time as that of PI. The relative changes in energy consumption and trip time (ΔSOC and ΔT) of ADMM to other methods are also presented in Fig. 5 for each road scenario.

Since the charging/discharging efficiency of the vehicle is less than 1, the regenerative braking is only able to regenerate a part of the consumed energy. Besides, moving the truck forward also consumes energy to overcome different kinds of resistances, and this energy consumption further reduces the efficiency of regenerative braking. Therefore, energy consumption can be reduced by avoiding any undesirable braking.

Fig. 5(a) shows that the HDT kept constant speed based on ADMM except during downhill stretches, where the truck decelerated first, then accelerated, and finally decelerated again to a constant speed. The ADMM-based energy consumption on the downhill was close to zero as shown in Fig. 5(b), which indicates that the truck moved forward in the most energy-conserving fashion with little undesirable braking, whereas more braking events were observed in Fig. 5(b) for all other methods, including the DP, PIC, and CC. Note that traditional trucks needed to downshift (decelerate) to increase the driving force when going uphill [see DP- and PIC-based speed trajectory in Fig. 5(a)], which caused the undesirable acceleration and braking on the downhill [see DP- and PIC-based energy consumption in Fig. 5(b)] to meet the trip-time requirement. Because the BE HDT powered by the motor was able to go uphill without decelerating and with a high speed, it left wider improvement space for improving energy consumption when going downhill than the traditional truck did. This phenomenon, which has never been revealed in the literature, indicates that the BE HDT adapts to the road topography in a more energy-efficient way than the ICE HDT does. In each case, the CC performed the worst since it used the most undesirable braking and thus consumed the most energy to keep a constant speed when going downhill. The energy consumption results in Fig. 5(b) show that, with a similar trip time, the ADMM-based BE HDT, respectively, consumed 1.72% and 1.78% less energy than the DP- and PIC-based ICE HDT and 1.93% less energy than the CC-based BE HDT.

Fig. 5(c) shows the optimal speed trajectories on a road with a long downhill segment where braking was inevitable for the BE HDT within the speed upper limit. In this case, the ADMM used less braking and thus consumed less energy than other methods did [Fig. 5(d)]. Obviously, the driving characteristics of BE HDT was quite different from that of the ICE-powered HDT. The energy consumption results show that the ADMM-based BE HDT, respectively, consumed 2.22% and 2.99% less energy than the DP- and PIC-based ICE HDT and 9.02% less energy than the CC-based BE HDT while keeping a similar trip time. Note that the reason that ADMM saves more energy than DP in the two cases is mainly due to the different vehicle types (e.g., BE HDT versus ICE HDT). The energy consumption values are expected to be similar if the two controllers are both developed for the BE HDT.

3) Performance Under Different Upper Speed Bounds: The speed upper bound was set to 90 km/h to follow the EU legal maximum speed limit. This speed limit can, however, be broken in some cases as the ICE HDT does in Fig. 5(c). Fig. 6 shows the optimization results under the upper speed bounds being set to 90, 92, and 95 km/h. For the case when the vehicle speed is generally less than the upper speed bound, the speed trajectories under different speed constraints are similar to each other [Fig. 6(a)], leading to similar energy consumption trajectories and thus similar relative changes of SOC reduction shown in Fig. 6(b).

For the case when the maximum speed corresponding to each scenario is reached, the speed trajectories are still similar to each other at other segments for reducing undesired braking [Fig. 6(c)]. Although the energy consumption with an upper speed bound of 90 km/h is a little smaller than those with different speed limitations, the energy consumption trajectories are still similar to each other [Fig. 6(d)], indicating the high performance of the ADMM-based controller against different upper speed bounds.

4) Performance With Vehicle Parameter Uncertainty: Because the models of battery and EM are simplified to constant efficiencies for constructing the vehicle energy consumption model, the performance of the ADMM controller against uncertain vehicle charge ($1/\beta^-$)/discharge (β^+) efficiencies is thus evaluated. The standard deviations of $1/\beta^-$ and β^+ are assumed to be 0.02 and 0.025, respectively. Also, the 3σ rule-based interval for $1/\beta^-$ and β^+ are, respectively, [0.74, 0.86] and [0.775, 0.925] under this assumption, indicating uncertainty of more than 15% for the discharge/charge efficiencies.

Ten sets of discharge/charge efficiencies were generated based on the assumed standard deviations. The ADMM controller operated on one efficiency set at each time and optimized the speed trajectory. The corresponding relative

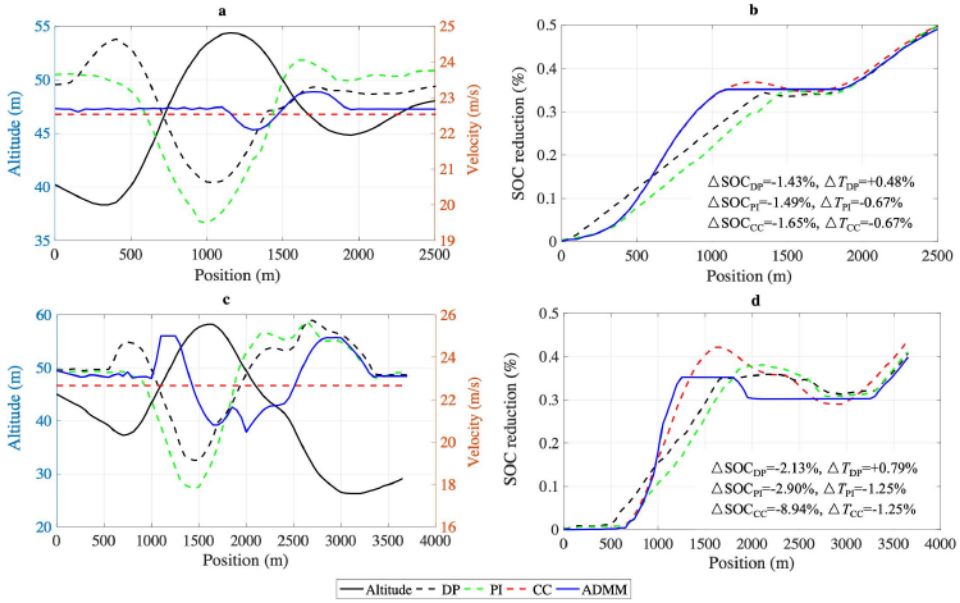

Fig. 5. Optimization results of truck speed. (a) and (c) Speed optimization results and the road altitude data, which, respectively, relates to [11, Figs. 7 and 9]. (b) and (d) Corresponding energy consumption, which is indicated by SOC reduction.

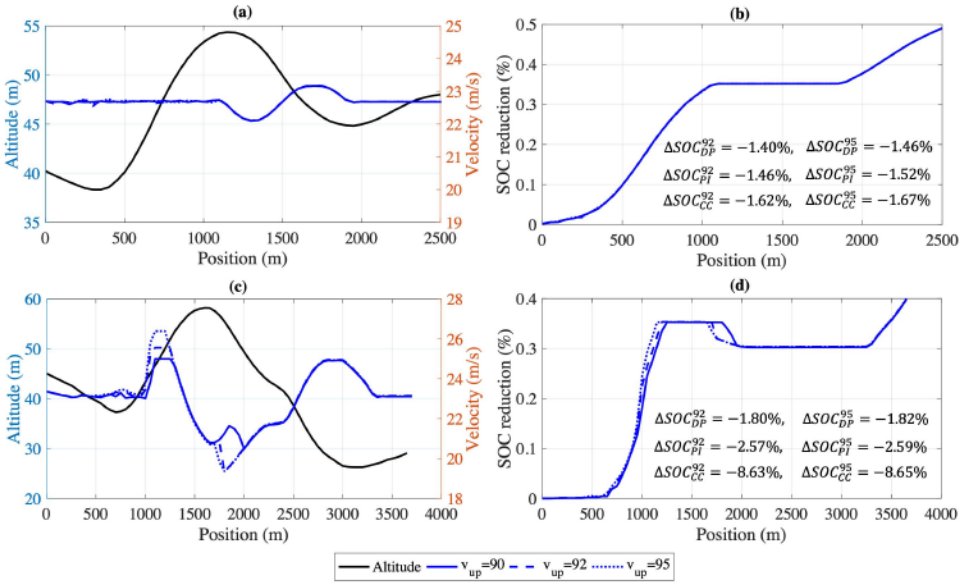

Fig. 6. Optimization results under different upper speed bounds. (a) and (c) Speed optimization results. (b) and (d) Corresponding energy consumption, which is indicated by SOC reduction.

changes of energy consumption on all ten efficiency sets were then obtained and the statistics with respect to different road topographies are presented in Fig. 7. Fig. 7(a) shows that the ΔSOC values are a little lower than those with the exact efficiencies for each comparison, and the 3σ variations are all within 0.1%. Fig. 7(b) shows similar comparison results with those using the exact efficiency values and the 3σ variations are all within 0.2%, which indicates the high robustness of the ADMM controller against uncertain vehicle parameters. This robustness of the ADMM controller validates the effectiveness of the energy consumption model of the truck derived in Section II for speed optimization purposes.

5) Performance Under Different Looking-Ahead Horizons: In practice, the prediction horizon can change according to the traffic, road topography, computation requirement, and so on. Generally, the longer the prediction horizon is, the more information that is gained from the future and the heavier the computation burden is. Fig. 8 shows the control results based on different looking-ahead horizons. The number following H indicates the number of segments N. For example, H20 indicates an N of 20 and the prediction horizon is thus 1000 m. Under each prediction horizon, the SOC reduction of the ADMM-based controller is compared with that of the CC-based controller and a relative change of

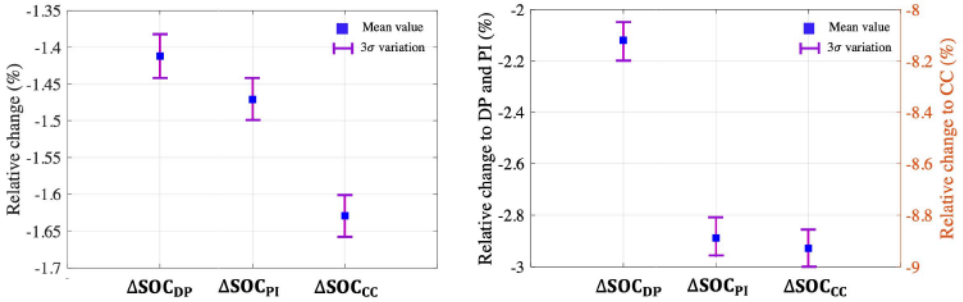

Fig. 7. Energy improvement under efficiency uncertainty based on the road topography in Fig. 5(a) (left) and (b) (right).

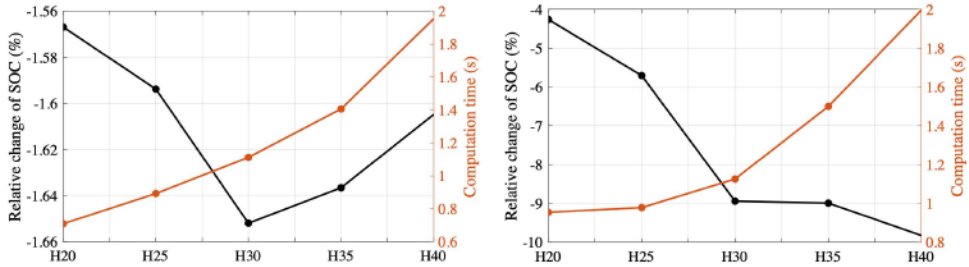

Fig. 8. Energy improvement and computation time under different looking-ahead horizons. The left subfigure presents the results with respect to the road topography in Fig. 5(a), while the right subfigure presents the results with respect to the road topography in Fig. 5(b). The black curve indicates the relative change of SOC and the red curve indicates the computation time for each case.

SOC is then deduced and presented in Fig. 8. Fig. 8 shows that the energy consumption generally decreases, while the computation time increases as the horizon increases. After H30, the relative change of SOC (absolute value) decreases a little in Fig. 8(a) and increases slowly in Fig. 8(b). Also, the computation times at H30 are both less than 1.2 s, which is lower than the maximum turnaround time of 2 s for real-time operation in this case. It is thus reasonable to set the number of segments to 30 in the simulation.

Note that if the looking-ahead road topography or traffic is uncertain, the prediction horizon may be reduced to improve the prediction confidence of the future information. In this research, it is assumed that the exact information of the traffic and road topography is known ahead.

B. Optimal Speed Control Under Traffic

As indicated before, the surrounding traffic can be introduced easily to the optimization $\mathcal{P}^{\mathrm{ME}}$. Appendix C shows the detailed modeling processes where the vehicle drives in a safe and energy-efficient way, and specifically, the upper speed limit $\bar{x}_i$ is adapted to the speed of the preceding vehicle.

1) Traffic Stochastic Modeling: Traffic around the truck needs to be simulated for traffic-based optimal speed control. Here, the exponential distribution was used to generate the stochastic traffic. The exponential distribution is a standard distribution that can model the interarrivals between vehicles [29]. Let events "1" and "0" represent, respectively, that there is a preceding vehicle or not. The traffic is a Markov process if the exponential distribution is used to represent the elapsed time between event "1" and "0" [30]. A continuous random variable X is said to have an exponential distribution if it has probability density function

$$f_X(x|\lambda) = \begin{cases} \lambda e^{-\lambda x}, & x > 0 \\ 0, & x \leq 0 \end{cases}$$

where $\lambda > 0$ is called the rate of the distribution. Here, X represents the traveling distance instead of the duration time as the distance and the duration time can always transform between each other in this case. X_1 is used to represent the traveling distances with preceding vehicles and X_2 is used to represent the traveling distances without preceding vehicles, and the mean values of these two distributions are thus $\mu_1 = 1/\lambda_1$ and $\mu_2 = 1/\lambda_2$. The traffic situation is decided by the values of μ_1 and μ_2. A large μ_1 and a small μ_2 indicate heavy traffic and vice versa. μ_1 and μ_2 can be calibrated based on available real traffic flow data.

2) Model Initialization: Some model parameters need to be initialized for defining the traffic characteristics. In this study, the minimum headway h_τ from the preceding vehicle was set to 1.2 s for the autonomous following trucks to ensure traffic safety [31]. The initial distance d_i from the preceding vehicle was assumed within [2, 4] s headway with uniform distribution, and the speed of the preceding vehicle v_p was assumed within [70, 80] km/h with uniform distribution. Heavy traffic is characterized by ($\mu_1 = 3$ and $\mu_2 = 2$). Light traffic is characterized by ($\mu_1 = 2$, $\mu_2 = 3$), and normal traffic is characterized by ($\mu_1 = 3$ and $\mu_2 = 3$). Note that in this case, the trip time τ is highly dependent on the traffic situations and thus cannot be determined in advance.

3) Speed Control Results With Traffic Involved: In this section, we first investigated the energy consumption results for trucks following a preceding vehicle on a flat road (road

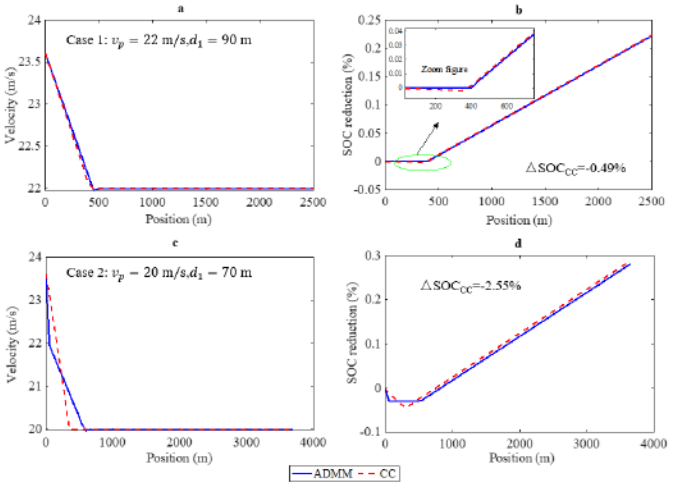

Fig. 9. Simulation results based on flat roads. (a) Speed trajectories based on ADMM and CC with a preceding vehicle velocity of 22 m/s and an initial spacing of 90 m. (b) SOC reductions as the position. (c) Speed trajectories based on ADMM and CC with a preceding vehicle velocity of 20 m/s and an initial spacing of 70 m. (d) SOC reductions as the position.

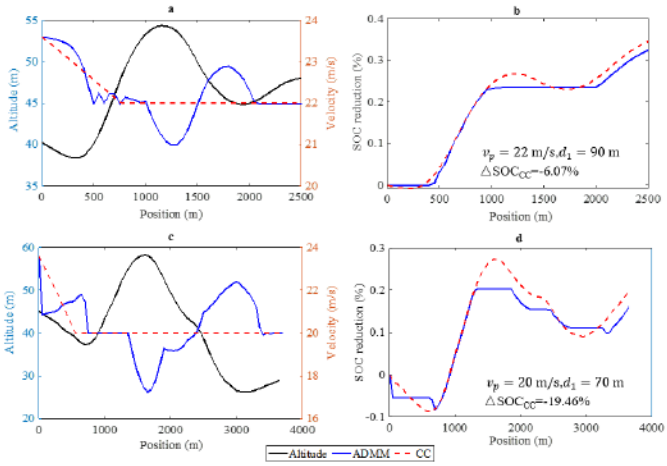

Fig. 10. Simulation results with both road slopes and traffic involved. (a) Speed trajectories and road altitude corresponding to Fig. 5(a). (b) SOC reductions. (c) Speed trajectories and road altitude corresponding to Fig. 5(c). (d) SOC reductions.

slope = 0). Then, we further investigated the truck energy consumption following a preceding vehicle on a road with varying slopes. Finally, the truck energy consumption results from Södertälje to Norrköping and the return were evaluated based on heavy and light traffic, respectively. In the scenarios with surrounding traffic involved, since no DP- or PIC-based speed trajectory can be introduced for comparisons, only the CC-based speed trajectory was used as a benchmark.

Fig. 9 shows the simulation results on flat roads with different velocities of the preceding vehicle and initial distances. Note that the CC speeds were obtained based on two rules: first, the CC travel time was the same as that based on ADMM, and second, the headway for CC was also set to 1.2 s. It was observed that the ADMM controller saved more energy than the CC did in both cases because the ADMM controller braked less on flat roads. In case 1, the ADMM used resistances (air and frictional) to decelerate, while the CC used additional braking, which thus consumed more energy. In case 2, the ADMM controller braked for a little while at first and then decelerated perfectly depending on resistances, whereas the CC controller braked until reaching the desired speed. Fig. 9 shows that our method still worked on saving energy for trucks following a preceding vehicle, and more energy was expected to be further saved with the road slopes involved.

Fig. 10 shows the simulation results with road slopes from Fig. 5. It was observed that the ADMM still braked less and was more energy-efficient. Fig. 10(b) and (d) shows that the energy consumption based on ADMM was, respectively, reduced by 6.07% and 19.46% compared to that based on CC. These results indicate that our method still performed excellently on energy consumption improvement for trucks following a preceding vehicle on roads with varying slopes.

Fig. 11 shows the statistical results under stochastic traffic from Södertälj to Norrköping and the return. For each direction, ten traffic scenarios covering heavy ($\mu_1 = 3$ and $\mu_2 = 2$), light ($\mu_1 = 2$ and $\mu_2 = 3$), and normal ($\mu_1 = 3$ and $\mu_2 = 3$) traffic were generated randomly and implemented to verify the performance of ADMM. For each traffic scenario, the preceding vehicle turns in and out randomly, and the total driving ranges with a preceding vehicle (labeled "Traffic") and without any preceding vehicles (labeled "No traffic") are listed in Table III. From Södertälj to Norrköping, Scenarios 1–3 indicate heavy traffic, Scenarios 4–7 indicate light traffic, and Scenarios 8–10 indicate normal traffic. For the return direction, Scenarios 1–4 indicate heavy traffic, Scenarios 5–7 indicate light traffic, and Scenarios 8–10 indicate normal traffic.

Under each traffic scenario, the relative change of energy consumption between ADMM and CC was calculated, and the mean values and 3σ variations were further obtained by summarizing the simulation results under different traffic scenarios. It was observed that from Södertälj to Norrköping, the energy consumption of ADMM was reduced by 4.05% with a 3σ interval being [3.27%, 4.83%] compared to that based on CC, while from Norrköping to Södertälj, the saved energy was up to 5.07% with a 3σ interval being [3.73%, 6.40%]. These results of energy saving indicate that our method adjusts well to different traffic situations for minimal energy consumption purposes.

V. Evaluation of Battery Aging Under Eco-Driving

Energy minimization is only one of the issues of BE HDT eco-driving control. The impact of driving algorithm on battery health is also relevant. Limited to the current battery technology, the battery life, which is generally shorter than the EV life [32], is even shorter for BE HDT due to the long-haul driving requirement. Therefore, battery aging in BE HDT needs not only to be online monitored but also to be further improved.

Indeed, many studies have been conducted on battery SOH estimation in recent years, e.g., Chen *et al.* [33] developed a promising method by using dual H infinity filters to estimate battery SOH in real time and the high estimation accuracy

TABLE III
DETAILS OF TEN TRAFFIC SCENARIOS

Direction	Label	S1(km)	S2(km)	S3(km)	S4(km)	S5(km)	S6(km)	S7(km)	S8(km)	S9(km)	S10(km)
Södertälj to	Traffic	77.7	69.75	70.65	44.7	48.3	40.15	42.7	49.1	56.45	51.35
Norrköping	No traffic	35.6	41.4	42.2	68.85	63.65	73.3	71.65	63.95	55.0	63.75
Norrköping	Traffic	72.7	61.5	69.7	78.45	35.5	45.2	40.15	58.15	55.55	56.65
to Södertälj	No traffic	40.9	49.15	44.45	35.8	80.5	67.4	72.85	59.2	61.35	60.65

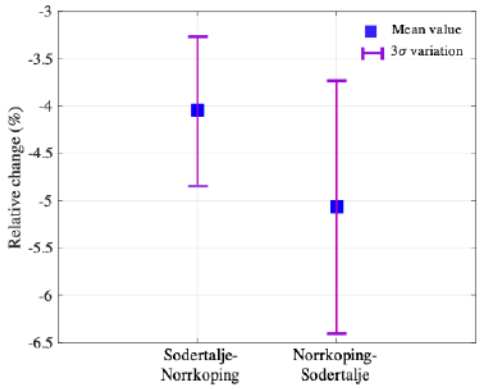

Fig. 11. Simulation results of energy consumption under stochastic traffic from Södertälj to Norrköping and the return.

was verified by the hardware-in-loop experiment, while there is limited literature on managing EV real-time operations for extending battery life. It is demonstrated here the positive effect of the proposed approach on battery aging.

A. EV Battery Life Model

Battery aging includes cycling aging and calendar aging [34]–[36]. For a long-haul BE HDT, one suitable operation mode would be shipping during the day and charging at night. This operation mode indicates that the truck battery pack will be cycled most of the day. In this case, it is only needed to evaluate the cycling aging of batteries for the BE HDT.

The battery cycling aging model used in this article is developed in [36]. This model is selected for two reasons. First, this model analyzes the effect of regenerative braking on battery aging and involves this effect in the aging model. Second, the model is verified by a large amount of experimental data simulating EV operations. The total capacity fade at a constant temperature is expressed as

$$\xi = \xi'\left(\mathrm{SOC}_{\mathrm{avg}}, \mathrm{SOC}_{\mathrm{dev}}\right) \times Q \tag{14}$$

where ξ is the total capacity fade, Q is the ampere-hour (Ah) charge processed during charging/discharging, and ξ' is the capacity fading rate and its unit is Ah faded per Ah processed by batteries. The capacity fading rate is expressed as

$$\xi' = k_1 \mathrm{SOC}_{\mathrm{dev}} e^{k_2 \mathrm{SOC}_{\mathrm{avg}}} + k_3 e^{k_4 \mathrm{SOC}_{\mathrm{dev}}} \tag{15}$$

where k_1–k_4 are four model fitting parameters. $\mathrm{SOC}_{\mathrm{avg}} = (1/(Q_{t1-t0})) \int_{Q_{t0}}^{Q_{t1}} \mathrm{SOC}(Q)\, dQ$ indicates the average SOC, with Q_{t0} being the amount of charge processed at the moment $t0$, Q_{t1} being the amount of charge processed at the moment $t1$, and $Q_{t1-t0} = Q_{t1} - Q_{t0}$. $\mathrm{SOC}_{\mathrm{dev}} = ((1/(Q_{t1} - Q_{t0})) \int_{Q_{t0}}^{Q_{t1}} (\mathrm{SOC}(Q) - \mathrm{SOC}_{\mathrm{avg}})^2\, dQ)^{1/2}$ indicates the normalized standard deviation from $\mathrm{SOC}_{\mathrm{avg}}$. It is assumed that the thermal management system of vehicle is able to keep the battery pack at a constant temperature of 25 °C and model parameters k_1–k_4 are thus initialized at this specific temperature [36].

B. Optimal Speed Control Impact on Battery Aging

1) Parameter Presetting of Simulation: The battery aging model indicates that, in general, the battery life is longer within the SOC cycling range of a lower SOC average value. Therefore, the ending SOC instead of the initial SOC is adjusted to the same value for each controller for fair comparisons. Generally, a long-haul HDT should run more than 500 km each working day. The road data from Södertälj to Norrköping and the return (about 240 km long) were thus repeated to generate the road data profile with the wanted travel distance. It was assumed that the truck shipped during the day and got charging at night. Slow charging was preferred for extending the battery life, and thus, the charging rate was set at 0.1 C in simulation. Note that the truck was expected to be used each working day, and thus, it would operate 260 days each year. Currently, the EV battery degradation limit is agreed upon 30% limit [32].

2) Battery Aging Without Traffic Involved: Here, three cases were simulated where for each case, the truck drove a predetermined distance or the battery pack reached a predetermined ending SOC each day.

Case 1: The truck traveled 800 km long each day, which is the Tesla claimed truck driving range with batteries fully charged. For fresh new battery packs, the battery (depths of discharge) DODs for the ADMM and CC benchmark were, respectively, 90.86% and 95.12% at the end of trip and the Ah throughputs of one battery pack were, respectively, 328.8 and 400.3 Ah. It was observed that, after speed control using ADMM, the charge delivered by battery was reduced by 71.5 Ah, which accounted for 22.9% of the battery nominal capacity (312.5 Ah). As the capacity degradation is proportional to the Ah throughput (see battery aging model), the ADMM controller was expected to reduce battery aging by more than 20% compared to the CC policy. This significant improvement showed that, when compared with the CC policy, the proposed eco-control algorithm not only minimized energy consumption but also extended battery life.

The improvement of battery health came from the fact that the proposed minimum energy control avoided undesirable braking. Note that the battery delivered about twice the

TABLE IV
BATTERY AGING AND LIFE ESTIMATION RESULTS FOR CASE 1

	SOC_{avg}	SOC_{dev}	$\delta\xi(\times 10^{-4}\text{Ah})$	ξ (%, one year)
CC	0.53	0.47	1.94	11.30
ADMM	0.50	0.45	1.64	8.36

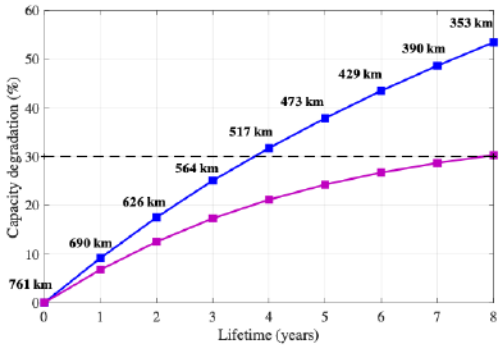

Fig. 12. Battery aging and life estimation results for Case 2 of ADMM (dark red line) and CC (blue line).

regenerative charge by each undesirable braking compared with the case when undesirable brakings were avoided.

In this case, the SOC cycling ranges for ADMM and CC benchmarks were [95.74%, 4.88%] and [100%, 4.88%], respectively. The battery aging evaluation results are presented in Table IV. It was surprising to find that the one-year-capacity fading ξ of battery based on ADMM was reduced by 35.2% compared to CC. The ADMM controller led to lower battery DOD and thus smaller SOC_{avg} and SOC_{dev} than the CC controller did. This low battery DOD caused a reduction of 15.5% on the capacity fading rate $\delta\xi$ using ADMM compared to using CC, which explains why ADMM reduced the capacity degradation of battery much higher than the aforementioned value of 20%.

Cases 2 and 3: Generally, an EV needs to be recharged when the battery SOC is lower than 10%–20%. Therefore, in Cases 2 and 3, the battery ending SOC for CC was, respectively, setting to 10% and 20%, which corresponds to a CC-based truck travel distance of 761 and 675 km each day for fresh new batteries. For fair comparisons, the driving range based on ADMM was set to the same value as that based on CC. Figs. 12 and 13 show the battery aging results for Cases 2 and 3, respectively, where the CC-based driving range within the corresponding DOD is also presented. It was observed that the driving range decreased as the battery capacity degraded. In Case 2 (Fig. 12), the CC- and ADMM-based battery lives were 3.74 years and 7.81 years long, respectively, indicating a life extension of 108.8% for the ADMM. At the battery end of life (EOL) for CC, the truck driving range decreased to about 517 km, equal to a range shrinkage of 32% compared to the initial driving range.

In Case 3 (Fig. 13), because the battery DOD was 10% shorter than that in Case 2, the CC- and ADMM-based battery lives were both longer and were about 6 years and 10.5 years long, respectively, indicating a life extension of 75% for ADMM. In this case, the reduction of driving range was

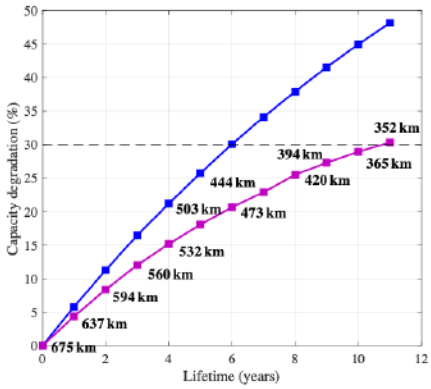

Fig. 13. Battery aging and life estimation results for Case 3 of ADMM (dark red line) and CC (blue line).

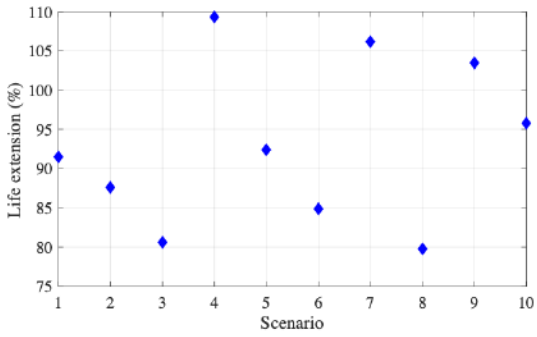

Fig. 14. ADMM-based life extension results under traffic.

equal to 202 km, which amounts to range shrinkage of up to 43%, indicated the necessity to reduce battery aging from EV driving perspectives.

3) Battery Aging Under Traffic: In this case, the optimal speed profiles under traffic were used, and as described before, the generated stochastic traffic scenarios from Södertälje to Norrköping and the return covered heavy, light, and normal traffic. For each scenario, the road altitudes and traffic from Södertälj to Norrköping and the return were connected and repeated to generate the desired road profiles for simulation, leading to totally ten simulated situations under different traffics. Fig. 14 shows the ADMM-based life extension results compared to CC for these ten traffic scenarios, where the CC-based ending SOC each day was set to 15% over different aging stages. The ADMM-based driving range each day was also set to the same value as that based on CC for fair comparisons. It was observed that the ADMM-based life extension ranged from 80% to 110%, with a mean value of up to 93.2%.

VI. CONCLUSION

This article has developed a methodology of controlling truck speed with minimal energy consumption and extended battery life. The novel state-space equations are constructed to describe the system dynamics of the truck. The dependencies of truck operation speed and energy consumption are captured by a state-space model with truck speed as the state and battery SOC as the output. An energy minimization problem is defined, where a novel optimization technique based on

the principle of ADMM is introduced for optimal solutions, coupled with an MPC strategy to deal with the uncertainty of the upcoming road topography and traffic for planning the truck speed in real time. The performance of the developed method is verified based on real highway altitudes between the cities of Södertälj and Norrköping in Sweden.

The simulation results show that the developed method is able to exploit topographical conditions for improved energy management, both in terms of minimizing total battery discharge and prolonging battery lifetime. It shows that the ADMM control consumes less energy under different scenarios than the DP control, PIC, and uniform speed CC. Generally, ADMM consumes 4%–5% less energy than CC does. It is surprising to find that ADMM generally extends battery life by more than 1 time than CC does. These results suggest the necessity to improve battery energy consumption and aging by optimizing truck speed trajectories. The battery energy and aging improvement values still hold when the traffic is introduced, which indicates that our method is also able to be used in electric buses and passenger EVs in urban driving.

Appendix A
EM Modeling

The EM is assumed to have similar efficiencies under traction and regenerative braking modes. The EM power P^{EM} is expressed as

$$P^{\mathrm{EM}} = \begin{cases} \dfrac{\pi n_m T^{\mathrm{EM}}}{30\eta\left(n_m, T^{\mathrm{EM}}\right)}, & \text{driving} \\ \dfrac{\pi n_m T^{\mathrm{EM}} \eta\left(n_m, T^{\mathrm{EM}}\right)}{30}, & \text{braking} \end{cases}$$

where T^{EM} indicates the EM torque, n_m indicates the rotational speed of the EM, and $\eta(n_m, T^{\mathrm{EM}})$ indicates the motor efficiency depending on n_m and T^{EM}. The EM efficiency map of the Tesla Semi is presented in Fig. 15 [37].

Remark: It was claimed that the Tesla Semi shares a number of parts with its Model 3, including the same motor [38] (Fig. 15).

The vehicle speed v and the EM rotational speed n_m is connected by

$$n_m = i_g \frac{30v}{\pi r_{\mathrm{whl}}}$$

where i_g indicates the gear ratio and r_{whl} indicates the radius of the vehicle wheel. Note that the truck speed on highway is limited within [75, 90] km/h [11]. In this case, the rotational speed range of EM is within [7000, 9000] r/min at a gear ratio of 19:1 [39]. Within this rotational speed range, the EM operates at a highly efficient mode with efficiencies being around 94%. Therefore, the EM efficiency can also be considered a constant when calculating the powertrain efficiency β_i.

Appendix B
Output Function Modeling

Four cases are considered here.

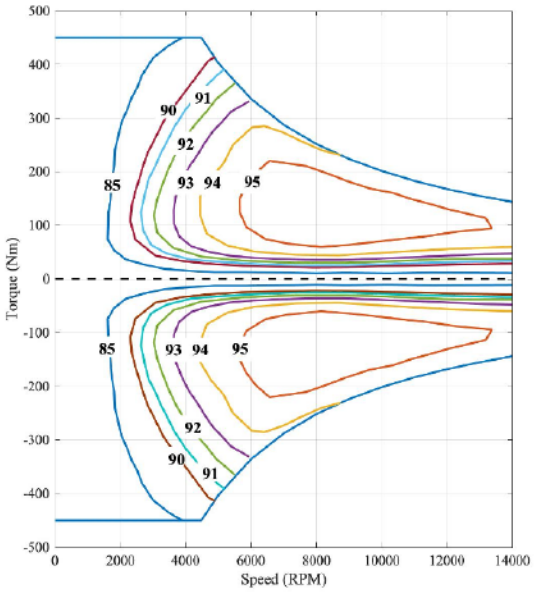

Fig. 15. EM efficiency map of Tesla Semi.

Case I: $F_i^{\mathrm{track}}(t) > 0$ within segment i, i.e., the battery always discharges. Note that since the term $1/UC$ in (3) is a constant, which will be removed temporarily for concise expression in the following derivations but will be added back in the simulation results:

$$\begin{aligned} G_i(x_i, a_i) &= \int_0^{T_i} p_i(t)\,dt = \int_0^{T_i} \frac{1}{\beta^+} v_i(t) F_i^{\mathrm{track}}(t)\,dt \\ &= \frac{ma_i + \beta_i^{(0)}}{\beta^+} \int_0^{T_i} (x_i + a_i t)\,dt \\ &\quad + \frac{\beta^{\mathrm{air}}}{\beta^+} \int_0^{T_i} (x_i + a_i t)^3\,dt \\ &= \frac{ma_i + \beta_i^{(0)}}{2a_i\beta^+}\left[(x_i + a_i T_i)^2 - x_i^2\right] \\ &\quad + \frac{\beta^{\mathrm{air}}}{4a_i\beta^+}\left[(x_i + a_i T_i)^4 - x_i^4\right] \\ &= \frac{1}{\beta^+}\left(ma_i + \beta_i^{(0)}\right) + \frac{\beta^{\mathrm{air}}}{\beta_+}\left(x_i^2 + a_i\right) \\ &= \gamma_i^{(0)} + \gamma_i^{(1)} a_i + \gamma_i^{(2)} x_i^2 \end{aligned} \tag{16}$$

where $\gamma_i^{(0)} = (\beta_i^{(0)}/\beta^+)$, $\gamma_i^{(1)} = ((m + \beta^{\mathrm{air}})/\beta^+)$, and $\gamma_i^{(2)} = ((\beta^{\mathrm{air}})/\beta^+)$.

Case II: $F_i^{\mathrm{track}}(t) < 0$ within segment i, i.e., the battery always charges. The derivation for Case I applies. Substituting β^+ by β^-, there is

$$G_i(x_i, a_i) = \gamma_i^{(0)} + \gamma_i^{(1)} a_i + \gamma_i^{(2)} x_i^2$$

where $\gamma_i^{(0)} = ((\beta_i^{(0)})/\beta^-)$, $\gamma_i^{(1)} = ((m + \beta^{\mathrm{air}})/\beta^-)$, and $\gamma_i^{(2)} = (\beta^{\mathrm{air}}/\beta^-)$.

Case III: The sign of F_i^{track} changes from positive to negative, i.e., there exists t_i^* such that

$$\begin{cases} F_i^{\mathrm{track}}(t) \geq 0, & t_i \leq t \leq t_i^* \\ F_i^{\mathrm{track}}(t) \leq 0, & t_i^* \leq t \leq t_{i+1}. \end{cases}$$

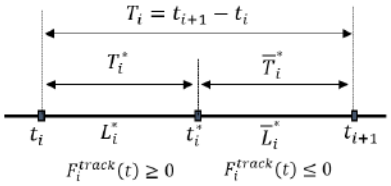

Fig. 16. Schematic: the track force is positive before t_i^* and then changes to negative after this moment.

Note that t_i^* is a function of (x_i, a_i). The schematic of this case is shown in Fig. 16.

The output function is the sum of two subsegments

$$G_i(x_i, a_i) = G_i^+(x_i, a_i) + G_i^-(x_i, a_i)$$

where

$$\begin{aligned} G_i^+(x_i, a_i) &= \int_{t_i}^{t_i^*} p_i(t)\, dt \\ &= \frac{ma_i + \beta_i^{(0)}}{\beta^+} \int_0^{T_i^*} (x_i + a_i t)\, dt \\ &\quad + \frac{\beta^{\text{air}}}{\beta^+} \int_0^{T_i^*} (x_i + a_i t)^3\, dt \\ &= \frac{ma_i + \beta_i^{(0)}}{2a_i\beta^+} \left[\left(x_i + a_i T_i^*\right)^2 - x_i^2 \right] \\ &\quad + \frac{\beta^{\text{air}}}{4a_i\beta^+} \left[\left(x_i + a_i T_i^*\right)^4 - x_i^4 \right] \end{aligned} \tag{17}$$

where $T_i^* = t_i^* - t_i$. Let the distance traveled when $p_i(t) > 0$ is L_i^*, and we have

$$L_i^*(x_i, a_i) = \int_0^{T_i^*} (x_i + a_i t)\, dt.$$

Following the state transition function (2), there is:

$$v_i\left(t^*\right) = x_i + a_i T_i^* = \sqrt{x_i^2 + 2a_i L_i^*}.$$

Substituting the above into (17), there is

$$\begin{aligned} G_i^+(x_i, a_i) &= \frac{L_i^*(x_i, a_i)}{\beta^+} \left(ma_i + \beta_i^{(0)}\right) \\ &\quad + \frac{L_i^*(x_i, a_i)\beta^{\text{air}}}{\beta^+} \left(x_i^2 + a_i L_i^*(x_i, a_i)\right) \\ &= \tilde{\gamma}_i^{(0)}(x_i, a_i) + \tilde{\gamma}_i^{(1)}(x_i, a_i) a_i + \tilde{\gamma}_i^{(2)}(x_i, a_i) x_i^2 \end{aligned}$$

where $\tilde{\gamma}_i^{(0)}(x_i, a_i) = ((L_i^*\beta_i^{(0)})/\beta^+)$, $\tilde{\gamma}_i^{(1)}(x_i, a_i) = (L_i^*/\beta^+)(m + \beta^{\text{air}} L_i^*)$, and $\tilde{\gamma}_i^{(2)}(x_i, a_i) = ((L_i^*\beta^{\text{air}})/\beta^+)$.

Here, it is emphasized that the coefficients $\tilde{\gamma}_i^{(0)}$, $\tilde{\gamma}_i^{(1)}$, and $\tilde{\gamma}_i^{(2)}$ depend on the vehicle state (x_i, a_i).

To compute $G_i^-(x_i, a_i)$, there is

$$\begin{aligned} G_i^-(x_i, a_i) &= \int_{t_i^*}^{t_{i+1}} p_i(t)\, dt \\ &= \frac{ma_i + \beta_i^{(0)}}{\beta^-} \int_0^{\bar{T}_i^*} \left(x_i^* + a_i t\right) dt \\ &\quad + \frac{\beta^{\text{air}}}{\beta^-} \int_0^{\bar{T}_i^*} \left(x_i^* + a_i t\right)^3 dt \end{aligned}$$

TABLE V
VALUE OF VECTOR PARAMETER γ_i UNDER DIFFERENT CASES

γ_i	Case I	Case II	Case III	Case IV
$\gamma_i^{(0)}$	$\frac{\beta_i^{(0)}}{\beta^+}$	$\frac{\beta_i^{(0)}}{\beta^-}$	$\frac{L_i^*\beta_i^{(0)}}{\beta^+} + \frac{\bar{L}_i^*\beta_i^{(0)}}{\beta^-}$	$\frac{L_i^*\beta_i^{(0)}}{\beta^-} + \frac{\bar{L}_i^*\beta_i^{(0)}}{\beta^+}$
$\gamma_i^{(1)}$	$\frac{m+\beta^{\text{air}}}{\beta^+}$	$\frac{m+\beta^{\text{air}}}{\beta^-}$	$\frac{L_i^*}{\beta^+}(m + \beta^{\text{air}} L_i^*) + \frac{\bar{L}_i^*}{\beta^-}\left[m + \beta^{\text{air}}\left(L_i^* + 1\right)\right]$	$\frac{L_i^*}{\beta^-}(m + \beta^{\text{air}} L_i^*) + \frac{\bar{L}_i^*}{\beta^+}\left[m + \beta^{\text{air}}\left(L_i^* + 1\right)\right]$
$\gamma_i^{(2)}$	$\frac{\beta^{\text{air}}}{\beta^+}$	$\frac{\beta^{\text{air}}}{\beta^-}$	$\frac{L_i^*\beta^{\text{air}}}{\beta^+} + \frac{\bar{L}_i^*\beta^{\text{air}}}{\beta^-}$	$\frac{L_i^*\beta^{\text{air}}}{\beta^-} + \frac{\bar{L}_i^*\beta^{\text{air}}}{\beta^+}$

where $\bar{T}_i^* = T_i - T_i^*$ and $x_i^* = v_i(t^*)$. The distance traveled when $p_i(t) < 0$ is

$$\bar{L}_i^*(x_i, a_i) = 1 - L_i^*(x_i, a_i) = \int_0^{\bar{T}_i^*} \left(x_i^* + a_i t\right) dt.$$

Again, there is

$$x_{i+1} = x_i^* + a_i \bar{T}_i^* = \sqrt{\left(x_i^*\right)^2 + 2a_i \bar{L}_i^*}.$$

Therefore, there is

$$\begin{aligned} G_i^-(x_i, a_i) &= \frac{\bar{L}_i^*}{\beta^-}\left(ma_i + \beta_i^{(0)}\right) + \frac{\bar{L}_i^*\beta^{\text{air}}}{\beta^-}\left[\left(x_i^*\right)^2 + a_i \bar{L}_i^*\right] \\ &= \frac{\bar{L}_i^*}{\beta^-}\left(ma_i + \beta_i^{(0)}\right) + \frac{\bar{L}_i^*\beta^{\text{air}}}{\beta^-}\left[x_i^2 + a_i\left(L_i^* + 1\right)\right] \end{aligned}$$

where the following fact was used:

$$x_i^* = x_i + a_i T_i^* = \sqrt{x_i^2 + 2a_i L_i^*}, \quad L_i^* + \bar{L}_i^* = 1.$$

Now, there is

$$G_i^-(x_i, a_i) = \bar{\gamma}_i^{(0)}(x_i, a_i) + \bar{\gamma}_i^{(1)}(x_i, a_i) a_i + \bar{\gamma}_i^{(2)}(x_i, a_i) x_i^2$$

where $\bar{\gamma}_i^{(0)}(x_i, a_i) = ((\bar{L}_i^*\beta_i^{(0)})/\beta^-)$, $\bar{\gamma}_i^{(1)}(x_i, a_i) = (\bar{L}_i^*/\beta^-)[m + \beta^{\text{air}}(L_i^* + 1)]$, and $\bar{\gamma}_i^{(2)}(x_i, a_i) = ((\bar{L}_i^*\beta^{\text{air}})/\beta^-)$.

Combining the two cases, there is

$$\begin{aligned} G_i &= G_i^+(x_i, a_i) + G_i^-(x_i, a_i) \\ &= \gamma_i^{(0)}(x_i, a_i) + \gamma_i^{(1)}(x_i, a_i) a_i + \gamma_i^{(2)}(x_i, a_i) x_i^2 \end{aligned} \tag{18}$$

where $\gamma_i(x_i, a_i) = \tilde{\gamma}_i(x_i, a_i) + \bar{\gamma}_i(x_i, a_i)$.

Case IV: The sign of F_i^{track} changes from negative to positive, i.e., there exists t_i^* such that

$$\begin{cases} F_i^{\text{track}}(t) \leq 0, & t_i \leq t \leq t_i^* \\ F_i^{\text{track}}(t) \geq 0, & t_i^* \leq t \leq t_{i+1}. \end{cases}$$

The derivation in this case follows the same as in Case III and thus shares the same expression for $G_i(x_i, a_i)$ as (18) with, however, different values of $\gamma_i^{(0)}$, $\gamma_i^{(1)}$, and $\gamma_i^{(2)}$.

Therefore, the sign of track force within segment i is determined by the vector (x_i, a_i), and the expressions of vector parameter γ_i under different cases are listed in Table V.

APPENDIX C
DERIVATION OF UPPER SPEED LIMIT

A safe headway between the truck and the preceding vehicle must be maintained all the time to ensure the driving safety, that is, the maximum permissible speed of the truck in the next segment must be limited according to the speed of the

preceding vehicle. The headway is defined as the time that elapses between the arrival of the leading vehicle and the following vehicle at the designated test point. Let us use h_τ to indicate the headway, and thus, there is

$$h_\tau = \frac{d}{v_f}$$

where d is the spacing between the two vehicles and v_f is the velocity of the following vehicle. To ensure the driving safety of the truck through segment i, there is

$$\begin{cases} \dfrac{d_i + T_i v_p - l}{x_{i+1}} \geq h_\tau \\ T_i = \dfrac{2l}{x_i + x_{i+1}} \end{cases} \tag{19}$$

where d_i is the spacing from the preceding vehicle at the beginning of segment i, l is the parameterized length of each road segment, and v_p is the velocity of the preceding vehicle and is assumed constant. Based on (19), then there is

$$\begin{cases} x_{i+1} \leq \dfrac{L_i - h_\tau x_i + \sqrt{(h_\tau x_i - L_i)^2 + 4h_\tau (L_i x_i + 2l v_p)}}{2h_\tau} = v_{\max}^{\mathrm{hw}} \\ x_{i+1} \geq 0 \geq \dfrac{L_i - h_\tau x_i - \sqrt{(h_\tau x_i - L_i)^2 + 4h_\tau (L_i x_i + 2l v_p)}}{2h_\tau} \end{cases} \tag{20}$$

where $L_i = d_i - l, i = 1, 2, \ldots, N$. Therefore, the maximum permissible value of x_{i+1} during optimization is $\bar{x}_{i+1} = \min(v_{\max}, v_{\max}^{\mathrm{hw}})$, where $v_{\max}$ is the legally maximum permissible speed in EU.

Acknowledgment

The authors would like to thank Dr. Hellström, Ford Motor Company, for kindly sharing the road altitude data between the cities of Södertälj and Norrköping in Sweden and the extensive discussions with engineers in Scania AB.

References

[1] D. C. Quiros, J. Smith, A. Thiruvengadam, T. Huai, and S. Hu, "Greenhouse gas emissions from heavy-duty natural gas, hybrid, and conventional diesel on-road trucks during freight transport," *Atmos. Environ.*, vol. 168, pp. 36–45, Nov. 2017.

[2] T. Earl, L. Mathieu, S. Cornelis, S. Kenny, C. C. Ambel, and J. Nix, "Analysis of long haul battery electric trucks in EU," in *Proc. Commercial Vehicle Workshop*, Graz, Austria, 2018, pp. 1–22.

[3] B. Sen, T. Ercan, and O. Tatari, "Does a battery-electric truck make a difference?—Life cycle emissions, costs, and externality analysis of alternative fuel-powered class 8 heavy-duty trucks in the United States," *J. Cleaner Prod.*, vol. 141, pp. 110–121, Jan. 2017.

[4] C. Tryggestad, N. Sharma, J. van de Staaij, and A. Keizer, "New reality: Electric trucks and their implications on energy demand," *McKensey Energy Insights*, 2017. [Online]. Available: https://www.mckinsey.com/industries/oil-and-gas/our-insights/a-new-reality-electric-trucks

[5] S. Sripad and V. Viswanathan, "Performance metrics required of next-generation batteries to make a practical electric semi truck," *ACS Energy Lett.*, vol. 2, no. 7, pp. 1669–1673, Jul. 2017.

[6] J. Lopez, D. G. Mackanic, Y. Cui, and Z. Bao, "Designing polymers for advanced battery chemistries," *Nature Rev. Mater.*, vol. 4, no. 5, pp. 312–330, May 2019.

[7] W. Dib, A. Chasse, P. Moulin, A. Sciarretta, and G. Corde, "Optimal energy management for an electric vehicle in eco-driving applications," *Control Eng. Pract.*, vol. 29, pp. 299–307, Aug. 2014.

[8] B. Xu *et al.*, "Cooperative method of traffic signal optimization and speed control of connected vehicles at isolated intersections," *IEEE Trans. Intell. Transp. Syst.*, vol. 20, no. 4, pp. 1390–1403, Apr. 2019.

[9] X. Zeng and J. Wang, "Globally energy-optimal speed planning for road vehicles on a given route," *Transp. Res. C, Emerg. Technol.*, vol. 93, pp. 148–160, Aug. 2018.

[10] A. A. Malikopoulos, S. Hong, B. B. Park, J. Lee, and S. Ryu, "Optimal control for speed harmonization of automated vehicles," *IEEE Trans. Intell. Transp. Syst.*, vol. 20, no. 7, pp. 2405–2417, Jul. 2019.

[11] E. Hellström, M. Ivarsson, J. Åslund, and L. Nielsen, "Look-ahead control for heavy trucks to minimize trip time and fuel consumption," *Control Eng. Pract.*, vol. 17, pp. 245–254, Feb. 2009.

[12] G. Guo and Q. Wang, "Fuel-efficient en route speed planning and tracking control of truck platoons," *IEEE Trans. Intell. Transp. Syst.*, vol. 20, no. 8, pp. 3091–3103, Aug. 2018.

[13] M. Held, O. Flardh, and J. Martensson, "Optimal speed control of a heavy-duty vehicle in urban driving," *IEEE Trans. Intell. Transp. Syst.*, vol. 20, no. 4, pp. 1562–1573, Apr. 2019.

[14] J. Borek, B. Groelke, C. Earnhardt, and C. Vermillion, "Economic optimal control for minimizing fuel consumption of heavy-duty trucks in a highway environment," *IEEE Trans. Control Syst. Technol.*, vol. 28, no. 5, pp. 1652–1664, Sep. 2019.

[15] V. Turri, B. Besselink, and K. H. Johansson, "Cooperative look-ahead control for fuel-efficient and safe heavy-duty vehicle platooning," *IEEE Trans. Control Syst. Technol.*, vol. 25, no. 1, pp. 12–28, Jan. 2017.

[16] M. P. Lammert, A. Duran, J. Diez, K. Burton, and A. Nicholson, "Effect of platooning on fuel consumption of class 8 vehicles over a range of speeds, following distances, and mass," *SAE Int. J. Commercial Vehicles*, vol. 7, no. 2, pp. 626–639, Sep. 2014.

[17] L. Tang, G. Rizzoni, and S. Onori, "Energy management strategy for HEVs including battery life optimization," *IEEE Trans. Transport. Electrific.*, vol. 1, no. 3, pp. 211–222, Oct. 2015.

[18] N. Sockeel, J. Shi, M. Shahverdi, and M. Mazzola, "Pareto front analysis of the objective function in model predictive control based power management system of a plug-in hybrid electric vehicle," in *Proc. IEEE Transp. Electrific. Conf. Expo (ITEC)*, Jun. 2018, pp. 1–6.

[19] X. Zhang, L. Guo, N. Guo, Y. Zou, and G. Du, "Bi-level energy management of plug-in hybrid electric vehicles for fuel economy and battery lifetime with intelligent state-of-charge reference," *J. Power Sources*, vol. 481, Jan. 2021, Art. no. 228798.

[20] N. Guo, X. Zhang, Y. Zou, L. Guo, and G. Du, "Real-time predictive energy management of plug-in hybrid electric vehicles for coordination of fuel economy and battery degradation," *Energy*, vol. 214, Jan. 2021, Art. no. 119070.

[21] M. Berecibar, M. Garmendia, I. Gandiaga, J. Crego, and I. Villarreal, "State of health estimation algorithm of $LiFePO_4$ battery packs based on differential voltage curves for battery management system application," *Energy*, vol. 103, pp. 784–796, May 2016.

[22] M. R. Amini, H. Wang, X. Gong, D. Liao-McPherson, I. Kolmanovsky, and J. Sun, "Cabin and battery thermal management of connected and automated HEVs for improved energy efficiency using hierarchical model predictive control," *IEEE Trans. Control Syst. Technol.*, vol. 28, no. 5, pp. 1711–1726, Sep. 2020.

[23] S. Boyd, N. Parikh, and E. Chu, *Distributed Optimization and Statistical Learning Via the Alternating Direction Method of Multipliers*. Norwell, MA, USA: Now Publishers, 2011.

[24] E. F. Camacho and C. B. Alba, *Model Predictive Control*. London, U.K.: Springer, 2013.

[25] P. Sahlholm, H. Jansson, E. Kozica, and K. H. Johansson, "A sensor and data fusion algorithm for road grade estimation," *IFAC Proc. Volumes*, vol. 40, no. 10, pp. 55–62, 2007.

[26] F. Ye, P. Hao, X. Qi, G. Wu, K. Boriboonsomsin, and M. J. Barth, "Prediction-based eco-approach and departure at signalized intersections with speed forecasting on preceding vehicles," *IEEE Trans. Intell. Transp. Syst.*, vol. 20, no. 4, pp. 1378–1389, Apr. 2019.

[27] D. Moser, R. Schmied, H. Waschl, and L. Del Re, "Flexible spacing adaptive cruise control using stochastic model predictive control," *IEEE Trans. Control Syst. Technol.*, vol. 26, no. 1, pp. 114–127, Jan. 2018.

[28] V. Turri, O. Flärdh, J. Mårtenssont, and K. H. Johansson, "Fuel-optimal look-ahead adaptive cruise control for heavy-duty vehicles," in *Proc. Annu. Amer. Control Conf. (ACC)*, 2018, pp. 1841–1848.

[29] K. Balakrishnan, *Exponential Distribution: Theory, Methods and Applications*. London, U.K.: Routledge, 2019.

[30] S. N. Ethier and T. G. Kurtz, *Markov Processes: Characterization and Convergence*, vol. 282. Hoboken, NJ, USA: Wiley, 2009.

[31] E. Nodine, A. Lam, M. Yanagisawa, and W. Najm, "Naturalistic study of truck following behavior," *Transp. Res. Rec.*, vol. 2615, no. 1, pp. 35–42, Jan. 2017.

[32] F. Yang, Y. Xie, Y. Deng, and C. Yuan, "Predictive modeling of battery degradation and greenhouse gas emissions from U.S. State-level electric vehicle operation," *Nature Commun.*, vol. 9, no. 1, pp. 1–10, Dec. 2018.
[33] C. Chen, R. Xiong, and W. Shen, "A lithium-ion battery-in-the-loop approach to test and validate multiscale dual H infinity filters for state-of-charge and capacity estimation," *IEEE Trans. Power Electron.*, vol. 33, no. 1, pp. 332–342, Jan. 2018.
[34] Y. Zhang, R. Xiong, H. He, X. Qu, and M. Pecht, "State of charge-dependent aging mechanisms in graphite/Li(NiCoAl)O_2 cells: Capacity loss modeling and remaining useful life prediction," *Appl. Energy*, vol. 255, Dec. 2019, Art. no. 113818.
[35] Y. Zhang, R. Xiong, H. He, X. Qu, and M. Pecht, "Aging characteristics-based health diagnosis and remaining useful life prognostics for lithium-ion batteries," *eTransportation*, vol. 1, Aug. 2019, Art. no. 100004.
[36] L. Lam and P. Bauer, "Practical capacity fading model for Li-ion battery cells in electric vehicles," *IEEE Trans. Power Electron.*, vol. 28, no. 12, pp. 5910–5918, Dec. 2013.
[37] MotorXP-PM. (2020). *Performance Analysis of the Tesla Model 3 Electric Motor using MotorXP-PM—Part 1*. [Online]. Available: https://motorxp.com/wp-content/uploads/mxp_analysis_TeslaModel3.pdf
[38] A. Davies. (2017). *Meet the Tesla Semitruck, Elon Musk'S Most Electrifying Gamble Yet*. [Online]. Available: https://www.wired.com/story/tesla-truck-revealed/
[39] K. Ritter. (2018). *Exploring the 'Hows' and 'Cans' of the Tesla Semi—Part 1*. [Online]. Available: https://insideevs.com/news/336239/exploring-the-hows-and-cans-of-the-tesla-semi-part-1/

Yongzhi Zhang (Member, IEEE) received the B.S. degree in vehicle engineering from Chongqing University, Chongqing, China, in 2013, and the Ph.D. degree in mechanical engineering from the Beijing Institute of Technology, Beijing, China, in 2019.

He was a Post-Doctoral Researcher with the Urban Mobility Group, Chalmers University of Technology, Gothenburg, Sweden. He has held visiting positions at the University of Maryland at College Park, College Park, MD, USA, and Mälardalen University, Västerås, Sweden. He is currently a Professor at the College of Mechanical and Vehicle Engineering, Chongqing University. His current research focuses on energy storage systems, including research on model-based battery management, degradation, and energy management for electric vehicles and grid storage.

Dr. Zhang was a recipient of the 2021 Best Vehicular Electronics Paper Award from the IEEE Vehicular Technology Society.

Xiaobo Qu (Senior Member, IEEE) is currently a Chair Professor of urban mobility systems with the Chalmers University of Technology, Gothenburg, Sweden. His research is focused on large, complex, and interrelated urban mobility systems. More specifically, his research has been applied to the improvement of emergency services, operations of electric vehicles and connected automated vehicles, and electric public transit systems.

Prof. Qu is a member of Academia Europaea—The Academy of Europe.

Lang Tong (Fellow, IEEE) received the B.E. degree from Tsinghua University, Beijing, China, in 1985, and the Ph.D. degree in electrical engineering from the University of Notre Dame, Notre Dame, IN, USA, in 1991.

He was a Post-Doctoral Researcher with the Information Systems Laboratory, Stanford University, Stanford, CA, USA. He has held visiting positions at Stanford University, the University of California at Berkeley, Berkeley, CA, USA, the Delft University of Technology, Delft, The Netherlands, and the Chalmers University of Technology, Gothenburg, Sweden. He is currently the Irwin and Joan Jacobs Professor of Engineering with Cornell University, Ithaca, NY, USA, and the Cornell Site Director of Power Systems Engineering Research Center. His current research focuses on data analytics, optimization, and economic problems in energy and power systems.

Dr. Tong was a recipient of the 1993 Outstanding Young Author Award from the IEEE Circuits and Systems Society, the 2004 Best Paper Award from the IEEE Signal Processing Society, the Young Investigator Award from the Office of Naval Research, and the 2004 Leonard G. Abraham Prize Paper Award from the IEEE Communications Society. He is a coauthor of eight student paper awards. He was a Distinguished Lecturer of the IEEE Signal Processing Society and the 2018 Fulbright Distinguished Chair in Alternative Energy.